

Received XX Month, XXXX; revised XX Month, XXXX; accepted XX Month, XXXX; Date of publication XX Month, XXXX; date of current version XX Month, XXXX.

Digital Object Identifier 10.1109/OJAP.2020.1234567

Sub-THz Conformal Lens Integrated WR3.4 Antenna for High-Gain Beam-Steering

Akanksha Bhutani*, Senior Member, IEEE, Joel Dittmer†, Student Member, IEEE, Luca Valenziano*, Student Member, IEEE, and Thomas Zwick*, Fellow, IEEE

¹*Institute of Radio Frequency Engineering and Electronics (IHE), Karlsruhe Institute of Technology, 76131 Karlsruhe, Germany

²†Institute of Photonics and Quantum Electronics (IPQ), Karlsruhe Institute of Technology, 76131 Karlsruhe, Germany

CORRESPONDING AUTHOR: Akanksha Bhutani (e-mail: akanksha.bhutani@kit.edu).

This work was financially supported by the Federal Ministry of Education and Research of Germany in the project "Open6GHub" (grant number: 16KISK010).

ABSTRACT This paper demonstrates the first conformal lens-integrated rectangular waveguide antenna that achieves high-gain beam-steering in the sub-THz range of 230 GHz to 330 GHz, to the best of the authors' knowledge. The antenna consists of a 2×32 array of elliptical slots (E-slots) fed by a standard WR3.4 rectangular waveguide, ensuring that the antenna operates in its dominant TE_{10} mode. The E-slots are spaced by less than half of the guided wavelength, which causes them to be fed with a constant phase difference, thus leading to a progressive phase shift along the antenna aperture. Consequently, the antenna main lobe steers from -71° to -16° as the operating frequency varies from 230 GHz to 330 GHz, respectively. The WR3.4 antenna gain is enhanced by integrating it with a conformal plano-convex parabolic lens. The conformal lens is designed taking into consideration the phase center of multiple steered beams, which leads to a significant gain enhancement of up to 10 dB over the complete beam-steering range. The conformal lens integrated WR3.4 antenna achieves a peak antenna gain of up to 30 dBi. An antenna prototype is manufactured using a mechanical assembly concept based on standard computerized numerical control (CNC) milling and a laser ablation process. For the prototype, a WR3.4 waveguide with an H-plane bend and a short termination is fabricated in a brass split-block module using CNC milling. The E-slots are ablated on a $125 \mu\text{m}$ thick aluminum (Al) sheet using a picosecond laser. Furthermore, a laser-structured die attach foil is interposed between the Al sheet and the brass split-block module to minimize the contact resistance between the E-slots and the WR3.4 waveguide. Additionally, a standard WR3.4 flange is manufactured to facilitate the antenna measurement. The conformal lens-integrated WR3.4 antenna has a compact size of $65 \text{ mm} \times 30 \text{ mm} \times 32.35 \text{ mm}$. It achieves the largest beam-steering range combined with the highest peak antenna gain in the broadband sub-THz range of 230 GHz to 330 GHz published to date.

INDEX TERMS CNC milling, conformal lens, elliptical slot, frequency beam-steering, laser ablation, parabolic, plano-convex, rectangular waveguide, sub-THz antenna, WR3.4.

I. INTRODUCTION

THE sixth generation (6G) of wireless communication aims to harness frequencies above 100 GHz to enable a wide range of applications that demand ultra-high data rates exceeding tens of gigabits per second. Although a large absolute bandwidth is available in the sub-THz range (i.e., from 100 GHz up to 1 THz), which is promising for achieving high data rates, the link budget poses significant challenges.

Even in a short line-of-sight (LOS) scenario spanning only a few meters, the free space path loss (FSPL) and atmospheric attenuation remain key concerns [1]–[3]. FSPL increases quadratically with frequency and distance, whereas atmospheric attenuation, which occurs due to absorption from oxygen, water vapor, and other gases, exhibits absorption maxima at specific frequencies. This leads to the so-called atmospheric attenuation windows, i.e., a range of frequencies

lying between two consecutive absorption maxima. An atmospheric attenuation window that exists between 200 GHz and 325 GHz is particularly attractive since it provides a good combination of factors, including a large bandwidth, atmospheric attenuation of less than 10 dB km^{-1} under fair weather conditions [4], and a variety of sub-THz sources including solid-state electronic and optoelectronic devices available in this frequency range [5], [6]. Additionally, the first IEEE-family standard for wireless communication in the sub-THz frequency range, IEEE Std. 802.15.3d, has been recently defined in the range of 253 GHz to 322 GHz [7]. The state-of-the-art sub-THz transmission experiments conducted in the recent past have employed solid-state electronic devices, such as frequency multipliers and power amplifiers, typically based on III-V semiconductors. Notable examples include a 240 GHz InGaAs mHEMT technology frontend used in a 64 Gbit s^{-1} LOS link spanning a distance of 850 m and a 96 Gbit s^{-1} LOS link covering a distance of 40 m [8]. Additionally, a 296 GHz InP HEMT technology frontend is used to establish a 120 Gbit s^{-1} LOS link over a distance of 9.8 m [9]. Alternatively, an optoelectronic device, such as a uni-traveling carrier photodiode, has been recently used to demonstrate a 200 Gbit s^{-1} LOS link over a distance of 52 m [10].

The compact size of these devices combined with their low conversion efficiency results in high power and current densities [11]. Consequently, minimizing internal power dissipation through adequate cooling, along with the elimination of undesired electromagnetic interference and the reduction of insertion loss, are major concerns when conducting such transmission experiments. This leads to a split-block waveguide-based package being the optimal choice for integrating these modules. Furthermore, the state-of-the-art sub-THz transmission links operating around 300 GHz, which have been demonstrated to date, are point-to-point links [8]–[10]. The antennas used in these experiments are waveguide horn antennas with WR3 input (i.e., a standard rectangular waveguide operating in its dominant TE_{10} mode in the 220 GHz to 325 GHz band). In these experiments, the gain of the waveguide horns is enhanced by integrating them with a polytetrafluoroethylene (PTFE) or high-density polyethylene (HDPE)-based plano-convex spherical lens. A waveguide horn radiates a broadside beam, and the axially-symmetric nature of a plano-convex spherical lens leads to beam collimation, thus enabling a point-to-point transmission link [8], [10].

The aforementioned wireless transmission links operate in the sub-THz range as point-to-point links (i.e., a transmitter sending data to a single receiver). However, 6G communication aims to establish a high data rate point-to-multipoint link (i.e., a transmitter sending data to multiple receivers) in the sub-THz range that extends over several meters [1]. This has not been demonstrated to date. To demonstrate a point-to-multipoint wireless link in the sub-THz range, multiple beams with high directivity (also known as "pencil

beams") and high spatial resolution to avoid mutual interference are necessary [1]. Thus, beamforming techniques are required. Two well-known beamforming techniques are analog and digital beamforming. Analog beamforming uses phase shifters to steer the beam of an array antenna in a desired direction and is commonly deployed in systems below 100 GHz. However, the implementation of a phase shifter in the sub-THz range leads to a relatively high insertion loss (e.g., a 250 GHz GaAs mHEMT phase shifter exhibits a mean insertion loss of 12 dB [12]). On the other hand, digital beamforming is challenging to implement in the sub-THz range due to its high circuit complexity, energy consumption, and operational costs [1]. In contrast, a sub-THz traveling-wave antenna or leaky-wave antenna is a simple and cost-effective solution to achieve beam steering by sweeping the center frequency in the sub-THz range. Among planar beam-steering antennas, a microstrip leaky-wave antenna operating from 230 GHz to 330 GHz, with a peak antenna gain of up to 11 dBi and a beam-steering range of -46° to 42° , is demonstrated in [13]. A modified version of this antenna is shown in [14] with a higher peak antenna gain of 13.7 dBi and a beam-steering range of -50° to 42° . Another example of a planar beam-steering antenna is a coplanar waveguide leaky-wave antenna operating from 220 GHz to 325 GHz, featuring a peak antenna gain of up to 13.5 dBi and a beam-steering range of -60° to 35° , as shown in [15]. Furthermore, a recent demonstration achieved 30 Gbit s^{-1} beam-steering wireless communication over a short distance of 50 cm using a 300 GHz optoelectronic transmitter and intradyne receiver link. This setup utilized a microstrip leaky-wave antenna [13], which is contacted by a sub-THz probe, which in turn is connected to a split-block medium power amplifier [16]. However, for outdoor applications covering longer distances of several meters, this setup becomes impractical. In order to establish a sub-THz point-to-multipoint wireless link operating in an outdoor environment, a sub-THz rectangular waveguide beam-steering antenna with the following specifications is required. First, the antenna should operate over the sub-THz range of 230 GHz to 330 GHz. The broad operating bandwidth is necessary to establish a high data rate wireless link in the sub-THz range. In addition, the operating bandwidth exploits the atmospheric attenuation window in this range and is also in line with the IEEE standard for wireless communication IEEE Std. 802.15.3d [7]. Second, the antenna should provide a large beam-steering range so that it can be used by a solid-state or optoelectronic transmitter module to transmit data to multiple receivers, which are separated from each other in the angular dimension. Third, the antenna should have high gain which compensates the FSPL and improves the link budget, thus ensuring that a sub-THz point-to-multipoint link operates over a distance of several meters. Finally, the antenna should have a WR3.4 standard rectangular waveguide input, allowing it to be easily connected to a solid-state device or optoelectronic sub-THz transmitter in a split-

block rectangular waveguide package. Among rectangular waveguide beam-steering antennas operating in the sub-THz range, very few works have been demonstrated to date, which are as follows. Firstly, a meandered rectangular waveguide structure realized using a silicon micromachining process combined with an array of 600 patch antennas is shown in [17]. This antenna operates from 230 GHz to 245 GHz (i.e., 6.32% relative bandwidth) with a measured beam-steering range of 48° and a measured gain of 28.5 dBi. Secondly, [18] presents a leaky-wave antenna consisting of eight slots in a gold-metallized silicon micromachined rectangular waveguide. This antenna operates from 288 GHz to 306 GHz (i.e., 6.06% relative bandwidth) with a simulated gain of 15 dBi. This paper demonstrates for the first time a rectangular waveguide beam-steering antenna operating over a large bandwidth of 230 GHz to 330 GHz (i.e., 35.7% relative bandwidth), to the best of the authors' knowledge. The antenna consists of an array of 2×32 elliptical slots (E-slots), which are manufactured by laser ablation on a $125\text{-}\mu\text{m}$ -thickness aluminum (Al) sheet. The E-slots are fed by a WR3.4 split-block waveguide, fabricated using computerized numerical control (CNC) milling. Thus, the process used in this work for manufacturing a prototype has a significantly lower cost compared to the silicon micromachining process employed in the previous works. The antenna shown in this work has a beam-steering range of 55° and a peak antenna gain of up to 19.5 dBi. Thus, the rectangular waveguide antenna presented in this work surpasses the previously shown sub-THz frequency beam-steering antennas in terms of a larger operational bandwidth, larger beam-steering range, and reduced manufacturing complexity.

Furthermore, the antenna is integrated with a conformal plano-convex parabolic lens, presented for the first time in this paper, to the best of authors' knowledge, which increases the peak antenna gain up to 30 dBi. The beam-steering integrated lens antennas (ILAs) shown to date either have a limited scan angle of around 20° [19] or those with larger scan angles of 60° or higher use a double-lens configuration [20] or a mechanical-scanning ILA [21]. These examples utilize plano-convex spherical lenses with additional complexity in terms of lens manufacturing, assembly, and alignment. Alternatively, a simpler solution employing a patch-fed planar dielectric slab lens is shown in [22], which has a limited scan angle of 27° . Note that no beam-steerable ILAs have been demonstrated in the sub-THz range, and hence this work shows the first 230 GHz to 330 GHz beam-steerable ILA with a large scan angle of 55° to the best of the authors' knowledge. The beam-steerable lens design uses a plano-convex cylindrical lens (i.e., commonly used in the optical domain to collimate light) as a starting point. The lens has a parabolic lens contour on one side, and its planar face on the opposite side is given a conformal shape to enable gain enhancement of multiple beams being radiated in different directions. The conformal shape takes the phase center of the rectangular waveguide

antenna into consideration, thus enabling a large scan angle of 55° without using double lenses or mechanical steering as shown in previous works [20], [21].

To summarize the novel contribution of this work, this paper presents the first sub-THz conformal lens integrated rectangular waveguide beam-steering antenna operating in the 230 GHz to 330 GHz range. The lens-integrated antenna is manufactured using relatively low-cost techniques of standard CNC milling and laser ablation. Furthermore, it achieves the largest operation bandwidth, widest beam-steering range and the highest peak antenna gain achieved by a sub-THz rectangular waveguide beam-steering antenna published to date. The paper is organized as follows. Section II describes the design procedure of a beam-steering WR3.4 antenna with an array of 2×32 E-slots. The electromagnetic (EM) simulation results of the beam-steering antenna are presented in this section. Section III outlines the design procedure of a conformal plano-convex parabolic lens, followed by the EM simulation results of the lens-integrated antenna. Section IV details the fabrication of the lens-integrated antenna prototype. The effects of manufacturing and assembly deviations are discussed in section V. Section VI presents the measurement results of the beam-steering antenna without and with the conformal lens. The measurement results are compared with the EM simulation results. Finally, a conclusion and future outlook of this work is presented in section VII.

II. E-SLOT WR3.4 ANTENNA DESIGN

A standard rectangular waveguide, WR3.4, with dimensions $a=864\text{ }\mu\text{m}$ and $b=432\text{ }\mu\text{m}$, is chosen for the antenna design, as the waveguide operates in its dominant TE_{10} mode within the desired frequency range of 230 GHz to 330 GHz. The cutoff wavelength of TE_{10} mode, given by $\lambda_c=2a$, is calculated as 1.728 mm, and the free space wavelength, given by $\lambda_0=c_0/f_0$ (where c_0 and f_0 denote the speed of light and frequency, respectively), is calculated as 1.07 mm at the center frequency of 280 GHz. Furthermore, the guided wavelength of TE_{10} mode, given by (1), is calculated as 1.365 mm at 280 GHz.

$$\lambda_g = \frac{\lambda_0 \lambda_c}{\sqrt{\lambda_c^2 - \lambda_0^2}}. \quad (1)$$

The waveguide antenna comprises a total of 2×32 E-slots cut into one of the broad walls of a WR3.4 waveguide as shown in the schematic in Fig. 1. The major axis of each E-slot is aligned parallel to the longitudinal axis of the WR3.4 waveguide, and the center of each E-slot is displaced from the longitudinal axis of the WR3.4 waveguide by an offset of x . The E-slots are placed periodically with an inter-element spacing of g . Furthermore, the consecutive E-slots are placed alternately on either side of the WR3.4 waveguide mid E-plane. The antenna is terminated with a waveguide short, placed at a distance, d from the last E-slot. The values of antenna dimensions are given in Table 1.

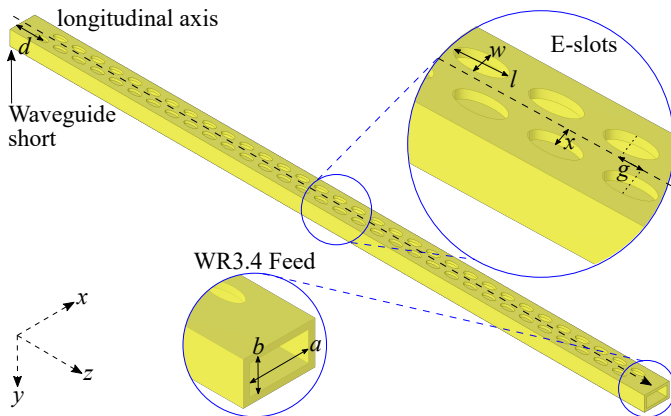


FIGURE 1: Schematic of a 2×32 E-slot rectangular waveguide WR3.4 antenna.

TABLE 1: Dimensions of 2×32 E-slot rectangular waveguide WR3.4 antenna.

a	b	l	w	x	g	d
864 μm	432 μm	550 μm	240 μm	200 μm	400 μm	900 μm

The design procedure used to determine these dimensions is described next. Each E-slot is a resonant radiating element. The E-slot length (i.e., the major axis length of an E-slot) is calculated as $\lambda_0/2$ at the center frequency of 280 GHz. This calculation results in an initial E-slot length of 535 μm . The slot width of a conventional slotted waveguide antenna with rectangular slots is typically around 0.2 times the slot length [23]. Therefore, the E-slot width (i.e., the minor axis length of an E-slot) is calculated as 107 μm . Using these calculated values as a starting point, the E-slot length and width are optimized based on EM simulation conducted in CST Studio Suite 2023 software. The optimization criteria used in this simulation are twofold. First, to increase the impedance matching bandwidth, i.e., achieve a reflection coefficient of less than -10 dB in the 230 GHz to 330 GHz range. Second, to enhance the peak antenna gain in the 230 GHz to 330 GHz range. The optimized E-slot length (l) and width (w) are obtained as 550 μm and 240 μm , respectively. The optimized l is close to the calculated l , whereas the optimized w is much larger than the calculated w . Fig. 2 shows the simulated reflection coefficient and peak antenna gain for the calculated and optimized E-slot width. In Fig. 2(a), the calculated w leads to a reflection coefficient of less than -10 dB from 250 GHz to 330 GHz, whereas the optimized w achieves a reflection coefficient of less than -10 dB over the 230 GHz to 330 GHz range. Hence, a larger E-slot width increases the impedance matching bandwidth by nearly 20 GHz. In Fig. 2(b), the optimized w results in 2 dB to 5 dB higher peak antenna gain in the 230 GHz to 250 GHz range. The gain bandwidth enhancement is achieved at the

cost of a slight degradation in the peak antenna gain around 280 GHz.

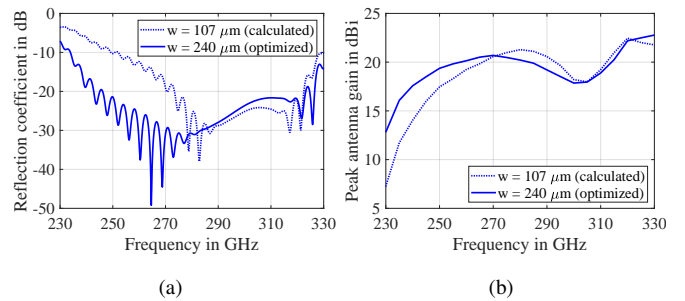


FIGURE 2: Influence of larger E-slot width on 2×32 E-slot WR3.4 antenna (a) Reflection coefficient. (b) Peak gain.

In order to design a beam-steering antenna over the target frequency range of 230 GHz to 330 GHz, the inter-element spacing between the E-slots should not be equal to $\lambda_g/2$. Note that if the inter-element spacing is kept as $\lambda_g/2$, the alternating E-slots are fed in phase, leading to broadside radiation. On the other hand, if the inter-element spacing is either less than or greater than $\lambda_g/2$, the E-slots are fed with a constant phase difference, leading to a progressive phase shift along the antenna aperture. The resulting phase front, i.e., the main lobe direction of the antenna, is inclined at an angle ϕ with respect to the broadside direction, as given by (2) [24].

$$\sin \phi = \frac{\lambda_0}{\lambda_g} - \frac{\lambda_0}{2g}. \quad (2)$$

Following the above-mentioned criterion, an inter-element spacing of $g=400$ μm (i.e., less than $\lambda_g/2$ at the maximum operating frequency of 330 GHz) is employed between the E-slots. Upon substituting the value of g into (2), a beam-steering range of 60.2° is calculated, with the main lobe of the antenna steering from -76.7° to -16.5° as the operating frequency changes from 230 GHz to 330 GHz, respectively. The negative sign indicates that the beam steers in angle from the near waveguide feed end towards the near broadside direction as the operating frequency is increased from 230 GHz to 330 GHz. Alternatively, if the inter-element spacing is increased to, for example, $g=500$ μm , the beam-steering range reduces to 37° (in this case, the main lobe steers from -40.3° to -3.3° in the 230 GHz to 330 GHz range). On the other hand, if the inter-element spacing is further reduced, it increases the mutual coupling between the E-slots; hence, an inter-element spacing of $g=400$ μm provides a good trade-off between a large beam-steering range and reduced mutual coupling among the E-slots. The E-slots are placed in shunt with the WR3.4 waveguide. Therefore, in order to achieve a good impedance matching over the 230 GHz to 330 GHz range, the waveguide admittance should be equal to the sum of the E-slot admittances.

The admittance of the dominant TE₁₀ mode in a WR3.4 waveguide is calculated by using (3) [25].

$$Y_0 = \frac{\beta}{k\eta} = \frac{\lambda_0}{\lambda_g \eta}. \quad (3)$$

In (3), $\eta=377\ \Omega$ and $k=2\pi/\lambda_0$ denote the intrinsic impedance and wavenumber of an air-filled waveguide, respectively, while $\beta=2\pi/\lambda_g$ denotes the propagation constant of the dominant TE₁₀ mode. The admittance of the E-slots is calculated in the following manner. The S -parameters of the waveguide with E-slots is simulated from 230 GHz to 330 GHz using a waveguide port excitation and free space boundary condition in CST Studio Suite 2023. In this simulation, the E-slot length and width are kept constant at 550 μm and 240 μm , respectively. Furthermore, the E-slot offset (x) with respect to the longitudinal axis of the WR3.4 waveguide is varied in steps of 120 μm , 160 μm , 200 μm , and 240 μm . The simulated S_{11} is used to determine the E-slot admittance by using (4) [26].

$$Y_{\text{slot}} = \frac{-2S_{11}}{S_{11} + 1}. \quad (4)$$

The reflection coefficient, ρ expressed in terms of the E-slot admittance normalized with respect to the waveguide admittance is given by (5). A broadband impedance matching of the 2×32 E-slot waveguide antenna implies that ρ and hence $1 - Y_{\text{slot}}/Y_0$ should be close to 0 over the desired 230 GHz to 330 GHz range.

$$\rho = \frac{1 - Y_{\text{slot}}/Y_0}{1 + Y_{\text{slot}}/Y_0}. \quad (5)$$

The real and imaginary part of the admittances (i.e., the conductance and susceptance, respectively) are analyzed separately. The real part of the waveguide admittance ($\text{Re}(Y_0)$) is equal to the waveguide conductance, G_0 is calculated using (3). The real part of the E-slot admittance ($\text{Re}(Y_{\text{slot}}$), i.e., E-slot conductance) is obtained from the above-mentioned S -parameter simulation followed by a S -parameter-to- Y -parameter conversion based on (4). Subsequently, the absolute value of the numerator of ρ (i.e., $|1 - \text{Re}(Y_{\text{slot}}/G_0)|$) is calculated over the target frequency range as shown in Fig. 3a. It is observed that as the E-slot offset (x) increases from 120 μm to 200 μm , the impedance matching bandwidth increases. However, as x is further increased to 240 μm , the impedance matching starts degrading. This happens because at a large offset, the E-slots are very close to the side wall of the WR3.4 waveguide, and the E-field intensity of the TE₁₀ mode approaches zero. Furthermore, the imaginary part of the E-slot admittance ($\text{Im}(Y_{\text{slot}}$), i.e., E-slot susceptance) obtained from S -parameter simulation followed by S -parameter-to- Y -parameter conversion based on (4) is shown in Fig. 3b. Note that the waveguide susceptance is zero at resonance ($\text{Im}(Y_0) = 0$) and hence not considered in this analysis. As shown in Fig. 3b, a negligible susceptance is observed as x is varied from 120 μm to 200 μm . Once again, a rise in susceptance is seen for $x=240\ \mu\text{m}$. The optimum

value of the E-slot offset obtained based on this analysis is $x=200\ \mu\text{m}$.

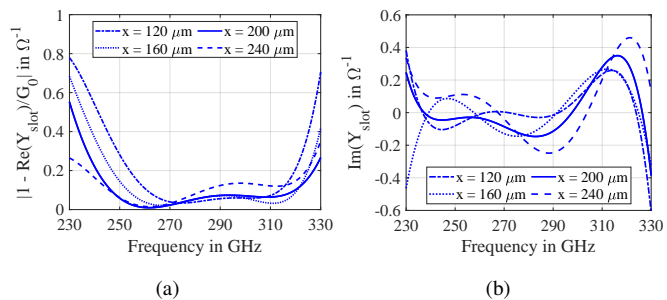


FIGURE 3: Influence of E-slot offset on matching the admittances of WR3.4 waveguide and 2×32 E-slots. (a) Real part of the E-slot and WR3.4 admittance i.e., conductance. (b) Imaginary part of the E-slot admittance i.e., susceptance.

The 2×32 E-slot waveguide antenna is terminated with a short. The waveguide short is placed at a distance of $d=920\ \mu\text{m}$ from the center of the last E-slot (i.e., nearly $0.75\lambda_g$ at the center frequency). Due to the large number of E-slots used in this antenna, the power reflected by the short termination is sufficiently small, and hence a spurious beam, which mirrors the main beam with respect to the broadside direction, is smaller than the sidelobe level of a uniformly-spaced E-slot waveguide antenna [27]. Finally, it is important to note that the broad wall thickness of the WR3.4 waveguide comprising the 2×32 E-slots should be a small fraction of the operating wavelength. Otherwise, if the broad wall has a significant thickness, each of the 2×32 E-slots will turn into stub waveguides that are parallel to the main feeding WR3.4 waveguide. The field inside these stub waveguides would be a superposition of higher-order TE modes, which will degrade the antenna performance [28]. In order to avoid this, a metal wall thickness of 125 μm is selected for the initial simulation model shown in Fig. 1. Later in section IV on prototype fabrication, only the topside broad wall of the WR3.4 waveguide comprising the 2×32 E-slots is manufactured by laser ablation of a 125 μm thickness Al sheet, and the remaining two side walls and the bottom broad wall of the WR3.4 waveguide are manufactured in a CNC-milled split-block module. The antenna model shown in Fig.1 is simulated with 2×16 and 2×32 E-slots to determine the influence of the number of E-slots on the reflection coefficient, peak gain, and beam-steering range of the antenna. The EM simulation results are shown in Fig.4.

The simulated reflection coefficient, S_{11} (Fig.4(a)), achieved using 2×32 E-slots shows a larger impedance matching bandwidth than achieved using 2×16 E-slots, i.e., the simulated S_{11} for 2×32 E-slots is less than $-10\ \text{dB}$ over the 230 GHz to 330 GHz range. The peak antenna gain achieved using 2×32 E-slots is nearly 3 dB higher than with 2×16 E-slots in the majority of the 230 GHz to 330 GHz

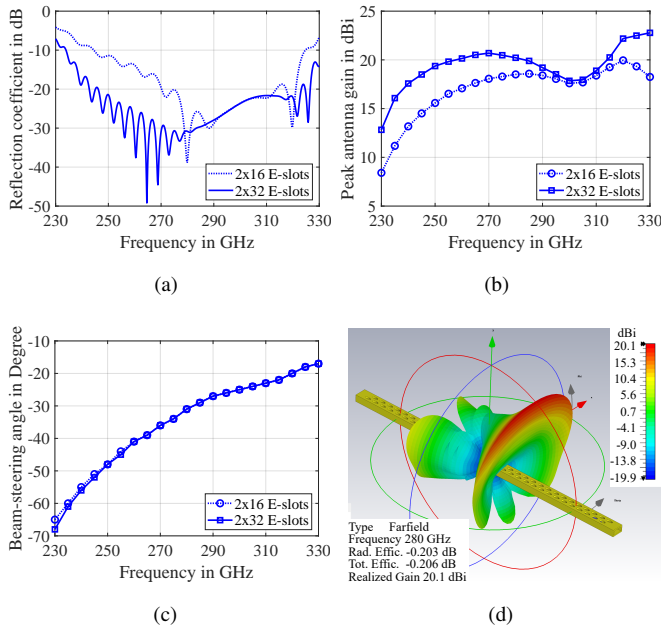


FIGURE 4: EM simulation of a 2×16 and 2×32 E-slot WR3.4 antenna. (a) Reflection coefficient. (b) Peak antenna gain. (c) Beam-steering angle. (d) Farfield radiation pattern of 2×32 E-slot WR3.4 antenna at 280 GHz.

range. This is understandable since a doubling in the number of radiation elements (i.e., E-slots) ideally increases the antenna gain by 3 dB. Note that around 300 GHz, the peak antenna gain achieved using 2×16 and 2×32 E-slots is nearly the same, since the WR3.4 waveguide is terminated in a short placed at a distance of around $0.75\lambda_g$ at this frequency. The traveling wave that gets reflected by the short end interferes destructively with the forward wave, which leads to a slight degradation in the peak antenna gain. This effect could be mitigated by using a matched waveguide termination. However, due to the manufacturing complexity associated with realizing a matched termination in the sub-THz range, a short waveguide termination is used in this work. The peak antenna gain can be further increased by approximately 3 dB by using 2×64 E-slots. However, this would enhance the manufacturing and assembly effort for such a large sub-THz antenna and is hence not pursued in this work. The beam-steering range shown in Fig.4(c) remains the same for both 2×16 and 2×32 E-slots. In both cases, the simulated beam-steering angle varies from -68° to -17° as the frequency increases from 230 GHz to 330 GHz, respectively, which closely matches the beam-steering range calculated using (2). Finally, Fig. 4(d) shows the simulated farfield radiation pattern of a 2×32 E-slot WR3.4 antenna at the center frequency of 280 GHz. A fan-shaped beam with a half power beamwidth (HPBW) of 3.3° in the H-plane (i.e., the longitudinal plane or the YZ plane as per Fig. 1) and 71.4° in the E-plane (i.e., the transversal plane

or the XY plane as per Fig. 1) of the antenna are observed. Furthermore, the simulated peak antenna gain is 20.1 dBi and the simulated total efficiency is 95.4%. The fan-shaped beam steers in the H-plane. The antenna beam points towards the waveguide feed end at 230 GHz and steers towards the broadside direction as frequency increases upto 330 GHz. The average simulated total efficiency of the antenna is around 85% in the 230 GHz to 330 GHz range.

III. CONFORMAL PLANO-CONVEX PARABOLIC LENS DESIGN

The directivity of an antenna, which radiates in a single direction (usually broadside) throughout its operational bandwidth, is enhanced by integrating it with a hemispherical or hemi-elliptical dielectric lens [19]. In this scenario, the dielectric lens geometry is axially symmetric, meaning it maintains the same cross-sectional view when rotated by any angle passing lengthwise through its focal point. To integrate an axially-symmetric dielectric lens with a broadside radiation antenna, there are two key points. Firstly, the focal point of the dielectric lens is vertically aligned with the antenna's phase center. Secondly, the vertical distance between the antenna's phase center and the dielectric lens focal point is adjusted depending on the type of lens used [19]. Consequently, the antenna beam is collimated in both E- and H-plane, thereby enhancing the directivity of a broadside-radiation antenna.

The 2×32 E-slot waveguide antenna beam differs from a broadside-radiation antenna beam in the following two aspects. First, it features a fan-shaped beam, where the HPBW of the antenna is significantly narrower in the H-plane compared to the E-plane (e.g., at 280 GHz, the HPBW is 3.3° and 71.4° in the H-plane and E-plane, respectively). Secondly, the antenna beam changes direction within its operational bandwidth i.e., the beam steers from -68° to -17° in the H-plane as the frequency increases from 230 GHz to 330 GHz, respectively. To enhance the directivity of such an antenna, a novel conformal plano-convex parabolic lens has been designed as shown in Fig. 5. The dielectric material used for the lens design is PTFE, commonly known as Teflon (The dielectric constant and loss tangent of Teflon at 300 GHz are $\epsilon_r=2.04$ and $\tan \delta=0.001$, respectively) [29]. The plano-convex parabolic lens cross-section of the lens is defined by three parameters, namely the lens thickness D_0 , the lens base width $2H$, and the lens radius of curvature R . The lens thickness and lens base width are selected as $D_0=8.16$ mm and $H=12.25$ mm. The lens radius of curvature R is determined using the equation of a parabolic curve given in (6) [30].

$$R = \frac{H^2}{2D_0}. \quad (6)$$

On substituting $D_0=8.16$ mm and $H=12.25$ mm into (6), R is calculated as 9.2 mm. From the basics of lens design theory, it is known that if the lens thickness is comparable

to the lens radius of curvature, as in this case, the lens is considered to be a thick lens. Furthermore, for a thick lens, the focal length f is given by (7) [30].

$$f = \left(\frac{R}{n-1} \right) \left(1 - \frac{D_0(n-1)}{nR} \right). \quad (7)$$

In (7), n denotes the refractive index of the lens material. Furthermore, the refractive index of PTFE is calculated using $n = \sqrt{\epsilon_r}$ as 1.43 at 300 GHz. Subsequently, the focal length, i.e., the distance between the phase center of the antenna and the base of the plano-convex parabolic lens, is calculated as $f = 16.4$ mm.

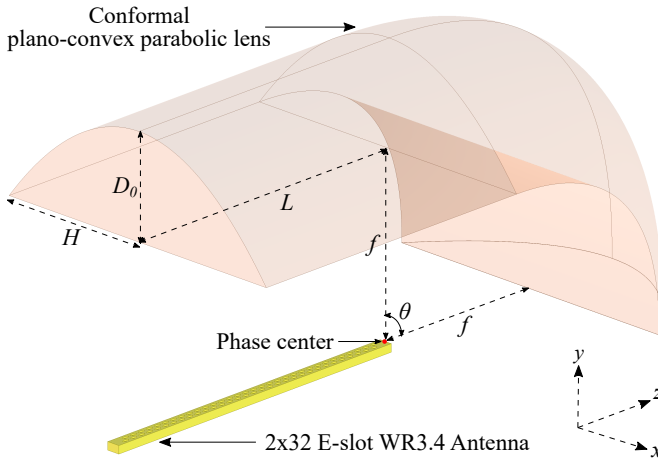


FIGURE 5: A conformal plano-convex parabolic lens and a 2×32 E-slot WR3.4 antenna in a simple free space simulation scenario.

The phase center of the 2×32 E-slot WR3.4 antenna is determined using EM simulations conducted in CST Studio Suite 2023. The phase center is estimated for multiple beams, ranging from 230 GHz (i.e., the beam points at -68° w.r.t. the broadside direction) to 330 GHz (i.e., the beam points at -17° w.r.t. the broadside direction) in intervals of 5 GHz. In each of these cases, the phase center lies close to the WR3.4 feed end. After determining the phase center, the plano-convex parabolic cross-section of the lens is extended by a length L along the z -axis until it is vertically aligned with the phase center of the 2×32 E-slot WR3.4 antenna. Using the phase center as the center of rotation, the XY cross-section of the plano-convex parabolic lens is rotated by $\theta=90^\circ$. Note that the perpendicular distance between the 2×32 E-slot WR3.4 antenna phase center and the plano-convex parabolic lens is kept constant as the focal length f at all points of the conformal lens. Consequently, unlike an axially symmetric dielectric lens that has a focal point, the conformal lens has a focal arc, whose perpendicular distance w.r.t. the 2×32 E-slot WR3.4 antenna phase center is always kept constant regardless of the beam's direction throughout the operational bandwidth of the antenna. The dimensions

used in the conformal lens integrated E-slot WR3.4 antenna assembly are provided in Table 2.

TABLE 2: Dimensions used in the conformal plano-convex parabolic lens integrated E-slot WR3.4 antenna assembly

D_0	H	R	f	L	θ
8.16 mm	12.25 mm	9.2 mm	14.4 mm	25 mm	90°

The conformal plano-convex parabolic lens is first simulated together with the 2×32 E-slot WR3.4 antenna in a simple free space scenario shown in Fig. 5. In this simulation, the lens and the antenna are positioned at a specific distance apart in free space. The lens and the antenna are aligned along the z axis. Furthermore, the lens is positioned at a distance equal to the focal length (f) from the phase center of the 2×32 E-slot WR3.4 antenna along the x and y axes. The practical integration of the conformal plano-convex parabolic lens and the 2×32 E-slot WR3.4 antenna is achieved using a split-block module whose fabrication and assembly are described in section IV.

The lens antenna free space assembly shown in Fig. 5 is simulated in CST Studio Suite 2023. A waveguide port with TE₁₀ mode excitation is used in this simulation. Fig. 6(a) compares the peak antenna gain of the 2×32 E-slot WR3.4 antenna with a conformal plano-convex parabolic lens (denoted as "with Lens") and the 2×32 E-slot WR3.4 antenna alone (denoted as "w/o Lens"). The maximum peak antenna gain "with Lens" is obtained using a focal distance of $f=14.4$ mm, which is very close to the value calculated using (7). It is observed that the simulated peak antenna gain "with Lens" ranges from 17 dBi at 230 GHz to 32.3 dBi at 330 GHz. The gain enhancement 'with Lens' in the 230 GHz to 250 GHz range is smaller than in the 270 GHz onwards range. This effect is attributed to the fact that the beam steers further away from the boresight direction in this range (see Fig. 6(b)). Furthermore, the conformal section of the lens is separated from the antenna by a fixed distance of f , as the phase center of all steered beams is approximated to be located at the midpoint of the WR3.4 feed end (see Fig. 5). This approximation leads to a smaller gain in the 230 GHz to 250 GHz range. The average gain achieved "with Lens" over the operational bandwidth of 230 GHz to 330 GHz is 26.6 dBi. Fig.6(b) compares the beam-steering angle of the "w/o Lens" and "with Lens" scenarios. It is observed that the conformal plano-convex parabolic lens has negligible influence on the beam-steering range of the 2×32 E-slot WR3.4 antenna. The simulated farfield radiation pattern of the lens antenna free space assembly at the center frequency, 280 GHz is shown in Fig. 6(c). On comparing the HPBW of the lens antenna with that of the antenna (see Fig. 4(d)), it is observed that the HPBW in the H-plane is practically the same as before, i.e., around 3° , whereas the HPBW in the E-plane changes from 71.4° to 2.9° . The H-plane cross-section of the lens contains the focal arc,

which maintains a constant focal distance to the 2×32 E-slot WR3.4 antenna phase center, thus enabling high-gain beam-steering along H-plane. This observation confirms that the conformal plano-convex parabolic lens enhances the antenna directivity by collimating the beam in the E-plane. The E-field distribution of the lens-antenna free space assembly in the beam collimation plane at 280 GHz is shown in Fig. 6(d). It is observed that the 2×32 E-slot WR3.4 antenna acts as a primary radiator that emits a spherical wave front and the conformal plano-convex parabolic lens transforms it into a planar wavefront. The combined aperture efficiency of the lens antenna (η_{ap}) is calculated using (8) [31].

$$\eta_{ap} = \frac{G}{\eta_{ant}\eta_L} \left(\frac{\lambda_0}{\pi L_D} \right)^2. \quad (8)$$

In (8), G denotes the simulated peak gain of the lens antenna assembly, L_D denotes the lens diameter illuminated by the 2×32 E-slot WR3.4 antenna beam width, η_{ant} denotes the simulated total antenna efficiency and η_L denotes the lens efficiency. At 280 GHz, using G , L_D , η_{ant} of 31.5 dBi, 20 mm and 85%, respectively and assuming η_L of 80% [32], the combined aperture efficiency of the lens antenna is estimated to be around 63%.

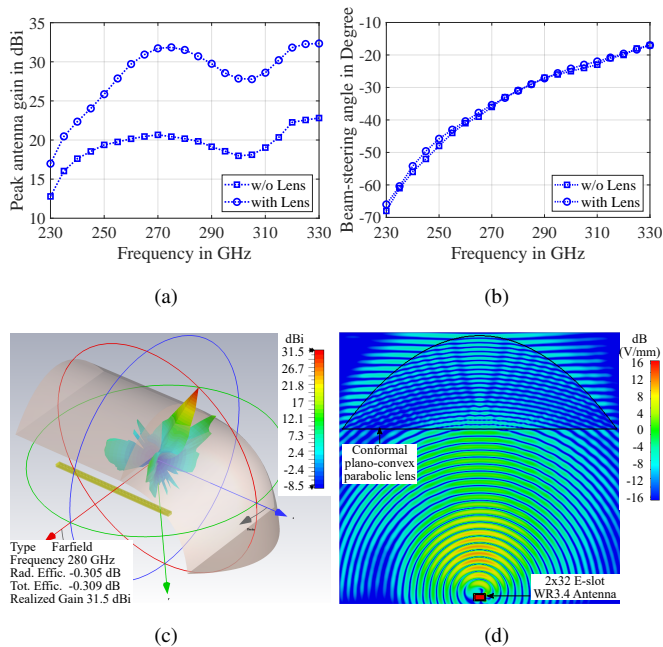


FIGURE 6: Free space assembly of a conformal plano-convex parabolic lens and a 2×32 E-slot WR3.4 antenna. (a) Simulated peak antenna gain with and without lens (b) Simulated beam-steering angle with and without lens. (c) Simulated far-field radiation pattern with lens at 280 GHz. (d) Simulated E-field in beam collimation plane of lens antenna free space assembly at 280 GHz.

IV. PROTOTYPE FABRICATION

A prototype of the 2×32 E-slot WR3.4 antenna, integrated with a conformal plano-convex parabolic lens, is realized using a manufacturing and assembly concept illustrated in Fig. 7. The manufacturing and assembly concept of the antenna comprise the following components. Firstly, a WR3.4 waveguide with an H-plane bend is fabricated in a brass split-block module using CNC milling. Unlike the simple simulation model shown in Fig. 1, an H-plane bend is included in the prototype to facilitate the integration of the conformal plano-convex parabolic lens and a standard WR3.4 flange (UG-387/U) for antenna measurement. The H-plane bend, along with the WR3.4 flange, is simulated separately to determine its influence on the antenna. The simulated S -parameters show a return loss greater than 35 dB and an insertion loss of less than 0.5 dB in the 230 GHz to 330 GHz range. Therefore, the bend has a negligible influence on the 2×32 E-slot WR3.4 antenna. The WR3.4 waveguide terminates with a waveguide short, manufactured as a separate CNC-milled metal block, which is then aligned and attached to the WR3.4 waveguide using alignment pins and mechanical screws, respectively. It's worth noting that manufacturing these two components in a single metal block would result in rounded corners at the WR3.4 termination due to the use of CNC milling. Alternatively, manufacturing these two components separately ensures precise corners at the WR3.4 termination, thereby achieving an ideal WR3.4 short. Secondly, the radiation elements of the antenna, i.e., the 2×32 E-slots, are fabricated on a $125 \mu\text{m}$ thick Al sheet using a laser ablation process. As previously explained in section II on antenna design, a small metal thickness for the broad wall of the WR3.4 waveguide comprising the 2×32 E-slots is necessary to ensure that the E-slots themselves do not act as stub waveguides in parallel to the feeding WR3.4 waveguide. This would degrade the beam-steering antenna performance due to a superposition of higher-order modes. For the remaining three walls of the WR3.4 waveguide, the metal thickness is not a critical factor, and hence they are manufactured using CNC milling as a split-block module. Furthermore, due to the small thickness of the Al sheet, a laser ablation process is preferred over the conventional CNC milling process for manufacturing the E-slots. A picosecond laser, LPKF ProtoLaser R4, with a laser wavelength of 515 nm, a maximum laser power of 8 W, and a focused laser beam diameter of $15 \mu\text{m} \pm 2 \mu\text{m}$ is used for this purpose. Thirdly, the picosecond laser is used to structure a $10 \mu\text{m}$ thick conducting foil, known as the die attach foil (DAF). In this step, the WR3.4 waveguide with an H-plane bend and a short termination is patterned on the DAF using a laser ablation process so that it replicates the WR3.4 waveguide structure on the CNC-milled split-block module beneath it.

The laser-structured DAF is interposed between the $125 \mu\text{m}$ thickness Al sheet containing E-slots and the split-block module containing the WR3.4 feeding waveguide. The usage of DAF in this assembly concept ensures that there is

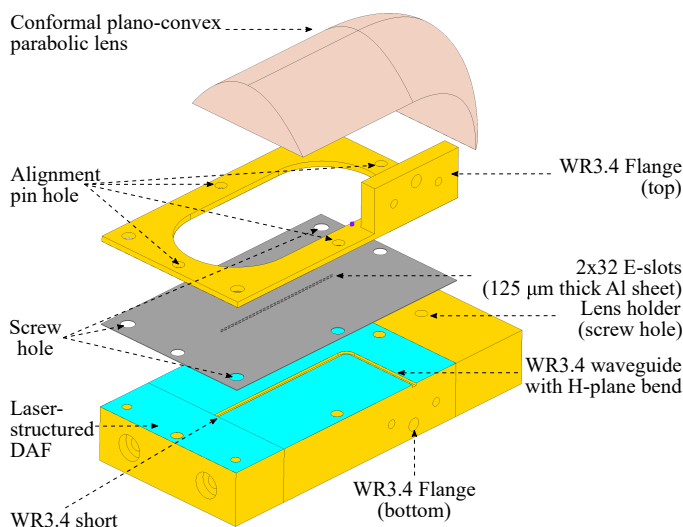
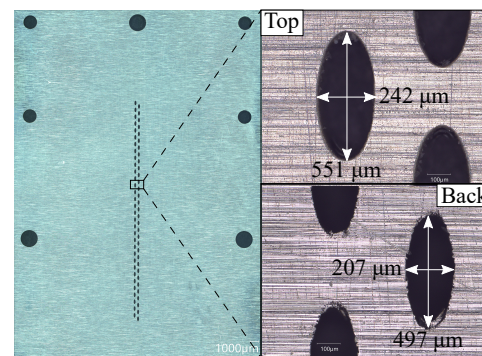


FIGURE 7: Manufacturing and assembly concept of a 2×32 E-slot WR3.4 antenna integrated with a conformal plano-convex parabolic lens.

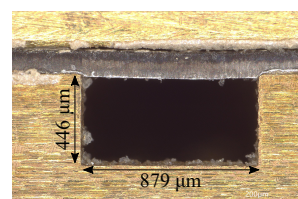
minimum contact resistance between the feeding waveguide and the radiating elements of the antenna. The DAF-based antenna assembly is cured at a temperature of 120°C for a duration of around 2 hours to ensure an airtight mechanical contact between the Al sheet containing 2×32 E-slots and the split-block module containing the WR3.4 feeding waveguide. Fourthly, to measure the antenna, a standard WR3.4 flange (UG-387/U) is necessary. The bottom half of the WR3.4 flange is realized in the CNC-milled split-block module containing the WR3.4 waveguide with H-plane bend. The top half of the WR3.4 flange is realized on a separate CNC-milled metal block placed on top. This metal block has a large opening in the middle centered with respect to the 2×32 E-slots. Furthermore, four alignment pins, one on each side of the assembly, are used to align the CNC metal blocks at the top and bottom. Additionally, three mechanical screws are used to connect the components. Finally, the conformal plano-convex parabolic lens is manufactured by CNC milling of a PTFE block. The lens is connected by a screw to the bottom CNC-milled metal block.

V. MANUFACTURING AND ASSEMBLY EFFECTS

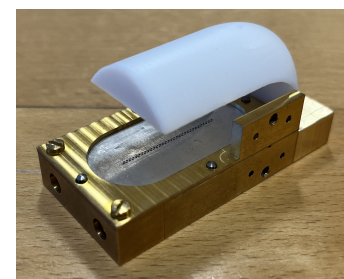
The manufacturing deviations of the 2×32 E-slots fabricated on the $125\ \mu\text{m}$ thick Al sheet are analyzed with a microscope (using a $300\times$ objective lens). A microscope photo of the laser-ablated 2×32 E-slots on the Al sheet is shown in Fig. 8a. The figure also displays the measured length and width of one of the E-slots as observed on the top and back sides of the Al sheet. It's important to note that "Top" refers to the side where the laser beam is focused and enters the Al sheet, while "Back" refers to the bottom side of the $125\ \mu\text{m}$ thick Al sheet through which the laser beam exits. It is observed that the E-slot length and width measured at the "Top"



(a)



(b)



(c)

FIGURE 8: (a) Microscope view of laser-ablated 2×32 E-slots on $125\ \mu\text{m}$ thick Al sheet. (b) Microscope view of CNC-milled WR3.4 waveguide. (c) A manufactured prototype of 2×32 E-slot WR3.4 antenna integrated with a PTFE-based conformal plano-convex parabolic lens.

show minute deviations of around $\pm 2\ \mu\text{m}$ from the desired values of $550\ \mu\text{m}$ and $240\ \mu\text{m}$, respectively. However, the E-slot length and width measured at the "Back" are $497\ \mu\text{m}$ and $207\ \mu\text{m}$, respectively, showing somewhat higher deviations from the desired values. These manufacturing deviations are caused by the natural divergence of a focused laser beam. This is why, when laser ablation is used to cut micro-mechanical contours, the walls of these contours cannot be perpendicular; instead, a kerf taper angle results depending on the laser parameters and material ablation depth [33]. The kerf taper angle leads to the E-slot length and width on the backside of the Al sheet being somewhat smaller than the desired values achieved on the top. The dimensions of multiple E-slots are inspected on the top and backside of the $125\ \mu\text{m}$ thick Al sheet, and similar observations are made in each of these cases. Additionally, the CNC-milled split-block module containing the WR3.4 waveguide with an H-plane bend is inspected using the microscope. A microscope photo of the CNC-milled WR3.4 waveguide cross-section is shown in Fig. 8b. The length and width of the manufactured WR3.4 waveguide are measured as $879\ \mu\text{m}$ and $446\ \mu\text{m}$, respectively, hence a slight deviation is observed compared to the standard WR3.4 waveguide length and width of $864\ \mu\text{m}$ and $432\ \mu\text{m}$, respectively. The above mentioned dimensions of the laser-

ablated E-slots and CNC-milled WR3.4 waveguide are used to modify the antenna simulation model shown in Fig. 6 to enable a fair comparison between the measurement and EM simulation results, which are shown and discussed in the next section. Due to the curved geometry of the conformal plano-convex parabolic lens, CNC milling is done from two sides by rotating the lens. This resulted in a slight manufacturing deviation of the lens prototype i.e., the planar surface of the lens prototype is slightly uneven. Furthermore, due to the small form factor of the lens, a single screw is used to fix the lens on the split block antenna module shown in Fig. 7. This implies that a minor rotation of the lens during the measurement could not be fully avoided. A photo of the 2×32 E-slot WR3.4 antenna integrated with a PTFE-based conformal plano-convex parabolic lens is shown in Fig. 8c. The length, width and height of this module are 65 mm, 30 mm and 32.35 mm, respectively.

VI. MEASUREMENT RESULT AND ANALYSIS

The manufactured prototype of the 2×32 E-slot WR3.4 antenna is measured using an antenna measurement setup. The working principle of this setup is described in detail in [34], [35] and illustrated in Fig. 9. Subsequently, the antenna is integrated with the PTFE-based conformal plano-convex parabolic lens and measured using the same setup.

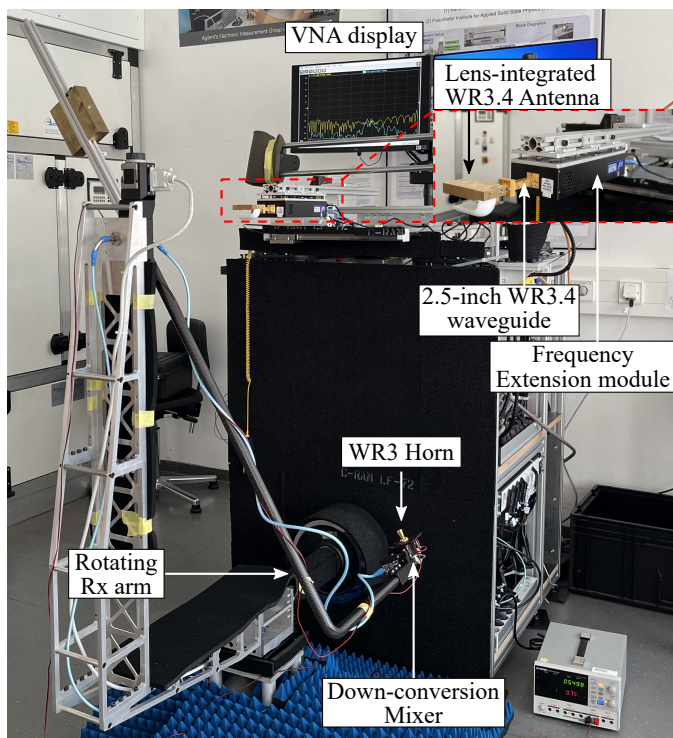


FIGURE 9: Sub-THz antenna measurement setup.

In this measurement setup, the 2×32 E-slot WR3.4 antenna prototype is connected via a 2.5-inch long WR3.4 waveguide to a frequency extension module (Model: WR3.4-VNAX), providing a frequency coverage of 220 GHz to

330 GHz. The input of this frequency extension module is connected to port 1 of a two-port vector network analyzer (VNA) (Model: Keysight PNA-X Network Analyzer N5242B) and a millimeter-wave controller (Model: Keysight N5261A). The antenna under test (AUT) acts as a transmitter (Tx) during the measurement. The second port of the millimeter-wave controller is connected to a receiver (Rx) module consisting of a WR3.4 down-conversion mixer, and a standard-gain WR3 horn with linear polarization and 25 dBi gain (as specified by the manufacturer). The Rx module is mounted on a motorized rotational arm. This arm is rotated around the AUT from -90° to 90° (see Fig. 9) in steps of 1° using a step motor. At each step, the forward transmission coefficient (S_{21}) is measured, thereby measuring a two-dimensional farfield radiation pattern of the AUT. The antenna measurement setup is calibrated before measuring the antenna characteristics. The calibration process includes an S -parameter calibration and a gain calibration. The S -parameter calibration is performed at the output of the 2.5-inch long WR3.4 waveguide using a WR3.4 calibration kit consisting of a waveguide short, a quarter-wave delay waveguide short, and a waveguide load. The calibration is performed from 220 GHz to 330 GHz with 801 frequency points and an IF bandwidth of 100 Hz. Subsequently, a gain calibration is performed by connecting a second standard-gain WR3 horn (25 dBi gain, linear polarization) to the 2.5-inch long WR3.4 waveguide followed by a WR3.4 split-block right-angle bend. During the gain calibration, the Tx and Rx standard-gain WR3 horn antennas are precisely aligned such that the Tx and Rx standard-gain horns are in each other's direct LOS and do not have any polarization mismatch. The forward transmission coefficient, S_{21} , is measured and the FSPL and the system losses are deduced. These losses are used to calibrate the measured AUT gain. After calibrating the antenna measurement setup, the 2×32 E-slot WR3.4 antenna prototype (at first without the lens and subsequently with the lens) is connected to the 2.5-inch long WR3.4 waveguide, and the reflection coefficient, beam steering angle, peak antenna gain, and farfield radiation pattern in the beam-steering plane are measured and compared with EM simulation as shown in Fig. 10 and Fig. 11. It should be noted that the simulation model used in this comparison includes the manufacturing deviations discussed in section V. This includes tapering of the 2×32 E-slots caused by the laser ablation process and deviation in the CNC-milled WR3.4 split-block waveguide.

The measured and simulated reflection coefficient of the antenna is shown in Fig.10a. It is observed that the measured reflection coefficient matches well with the simulation. Furthermore, the measured reflection coefficient is less than -15 dB over the target range of 230 GHz to 330 GHz. As previously mentioned, the Rx module mounted on the arm is rotated around the AUT from -90° to 90° to measure the two-dimensional farfield radiation pattern in the beam-steering plane (i.e. H-plane) of the AUT. Note that the

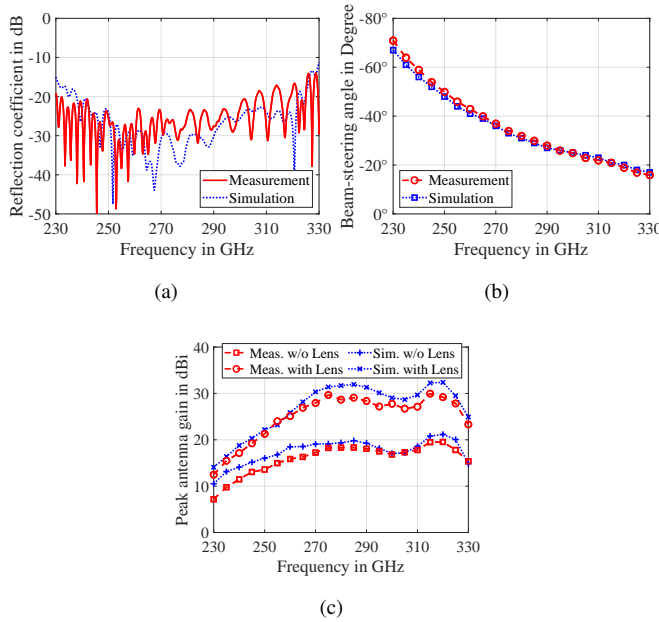


FIGURE 10: Measurement and EM simulation result of 2×32 E-slot WR3.4 antenna without and with a conformal plano-convex parabolic lens. (a) Reflection coefficient. (b) Beam-steering angle. (c) Peak antenna gain without and with lens.

farfield radiation pattern of the antenna cannot be measured in the E-plane of the antenna due to the mechanical restriction imposed by the antenna measurement setup shown in Fig. 9. The measured data is used to calculate the peak antenna gain and the beam-steering angle of the AUT. Note that the angle corresponding to the peak antenna gain in the beam-steering plane is determined as the beam-steering angle of the AUT. The measured and simulated beam-steering angle of the AUT is shown in Fig. 10b. Both measured and simulated values are determined from 230 GHz to 330 GHz in steps of 5 GHz. The measured and simulated beam-steering angle match well with each other. The measurement shows that the AUT beam steers from -71° to -16° as the frequency is swept from 230 GHz to 330 GHz, respectively.

The reflection coefficient and the beam-steering angle measurement result for the 2×32 E-slot WR3.4 antenna with and without the conformal plano-convex parabolic lens are very similar to the results shown in Fig. 10a and Fig. 10b, respectively, and hence shown only once. The peak antenna gain of the 2×32 E-slot WR3.4 antenna with and without the conformal plano-convex parabolic lens are measured and compared with the corresponding EM simulation result as shown in Fig. 10c. Once again, a good match is observed between the measurement and simulation. The measured peak antenna gain of the 2×32 E-slot WR3.4 antenna (without the lens) shows a median value of 17.2 dBi and a maximum value of 19.5 dBi. After integrating the conformal

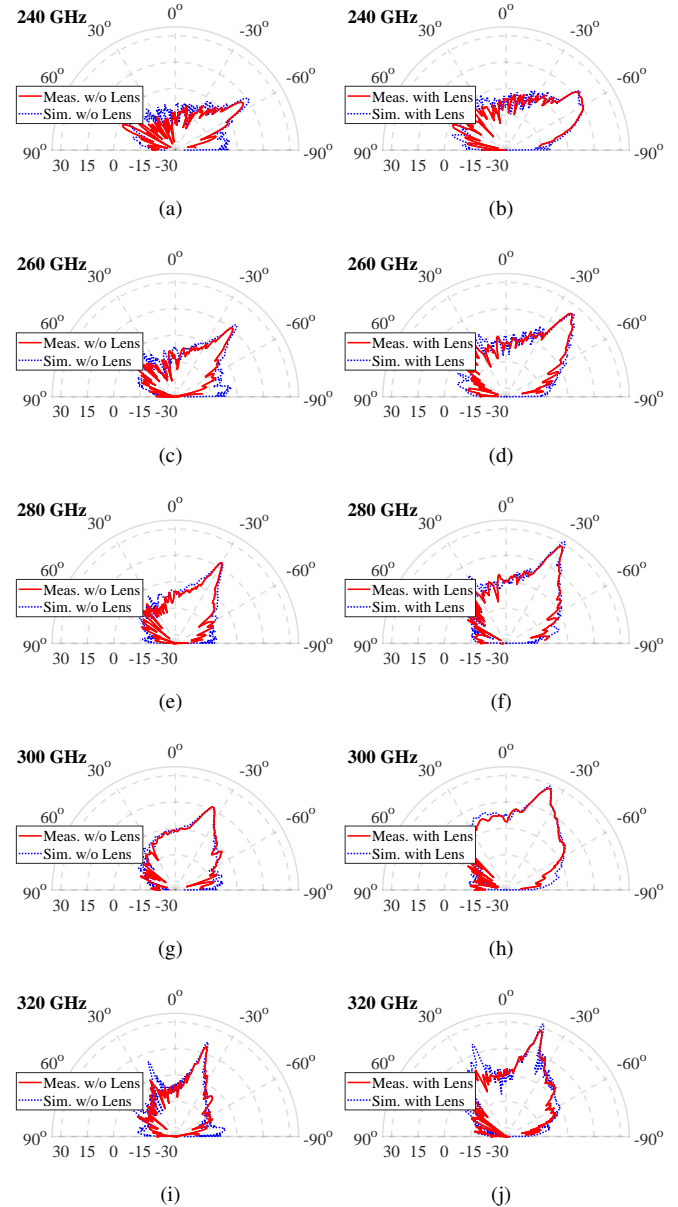


FIGURE 11: Measured and simulated farfield radiation pattern of 2×32 E-slot WR3.4 antenna without and with a conformal plano-convex parabolic lens. (a) 240 GHz without lens. (b) 240 GHz with lens. (c) 260 GHz without lens. (d) 260 GHz with lens. (e) 280 GHz without lens. (f) 280 GHz with lens. (g) 300 GHz without lens. (h) 300 GHz with lens. (i) 320 GHz without lens. (j) 320 GHz with lens.

plano-convex parabolic lens, the measured peak antenna gain shows a median value of 27.1 dBi and a maximum value of 30 dBi. The difference in the measured and simulated gain for the lens integrated antenna is attributed to the effects of manufacturing and assembling the lens prototype, which are described in section V. Furthermore, the conformal plano-convex parabolic lens enhances the peak antenna gain

TABLE 3: Comparison with state-of-the-art sub-THz beam-steering antennas.

Reference	Frequency range	Bandwidth	Antenna type	Manufacturing	Peak gain	Beam-steering
[13]	230 - 330 GHz	35.7%	Planar (microstrip)	Lithography	11 dBi	-46° to 42°
[14]	230 - 330 GHz	35.7%	Planar (microstrip)	Lithography	13.7 dBi	-50° to 42°
[15]	220 - 325 GHz	38.5%	Planar (coplanar waveguide)	Lithography	13.5 dBi	-60° to 35°
[17]	230 - 245 GHz	6.3%	Rectangular waveguide + patch array	Silicon micromachining	28.5 dBi	-24° to 24.5°
[18]	288 - 306 GHz	6.1%	Rectangular waveguide	Silicon micromachining	15 dBi*	-
This work	230 - 330 GHz	35.7%	Rectangular waveguide + Conformal lens	CNC milling + Laser ablation	30 dBi	-71° to -16°

*Only simulated value is given in the paper.

between 5 dB and as high as 10 dB in the target range of 230 GHz to 330 GHz. The measured and simulated farfield radiation pattern in the beam-steering plane of the 2×32 E-slot WR3.4 antenna without and with the conformal plano-convex parabolic lens are shown in Fig. 11. These farfield radiation patterns are shown at 240 GHz, 260 GHz, 280 GHz, 300 GHz, and 320 GHz, and the change in beam-steering angle with the frequency is visible in these plots. The gain enhancement achieved with the lens is also visible when comparing the farfield radiation pattern of the 2×32 E-slot WR3.4 antenna without and with the conformal plano-convex parabolic lens at any of these frequencies. The measured side lobe level (SLL) of the antenna integrated with and without the lens over the 230 GHz to 330 GHz range is shown in Fig. 12. At each frequency, the measured SLL is normalized with respect to the corresponding peak antenna gain. For both the antenna and the lens-integrated antenna, the best SLL is around 20 dB below the peak gain, which is achieved around the center frequency. Furthermore, the SLL increases up to around 10 dB below the peak gain as the frequency approaches the lower and upper edges of the target frequency range.

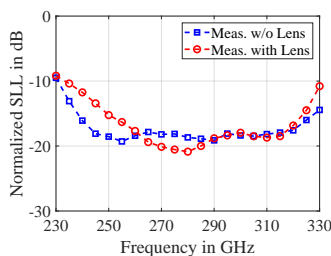


FIGURE 12: Measured normalized side lobe level of 2×32 E-slot WR3.4 antenna without and with conformal plano-convex parabolic lens.

Table 3 compares the performance of the conformal plano-convex parabolic lens integrated 2×32 E-slot WR3.4 antenna with state-of-the-art sub-THz beam-steering antennas demonstrated in the same frequency band. On comparison with the state-of-the-art planar (i.e., microstrip and coplanar waveguide) and rectangular waveguide beam-steering antennas operating in the same sub-THz band, this work

achieves the highest peak antenna gain of 30 dBi achieved in the 230 GHz to 330 GHz range. Furthermore, among the rectangular waveguide beam-steering antennas operating in the same sub-THz band, this work demonstrates the largest beam-steering range of -71° to -16° and the widest operational bandwidth of 230 GHz to 330 GHz (i.e., 35.7% relative bandwidth). It is noteworthy that the manufacturing techniques used in this work consist of standard CNC milling and laser ablation, which are relatively low cost compared to the high-precision silicon micromachining employed in previously demonstrated sub-THz rectangular waveguide beam-steering antennas.

VII. CONCLUSION AND FUTURE OUTLOOK

This paper presents the first sub-THz conformal lens-integrated rectangular waveguide antenna that achieves the largest beam-steering range and the highest peak antenna gain in the broadband frequency range of 230 GHz to 330 GHz published to date. The antenna consists of a 2×32 array of E-slots spaced by less than half of the guided wavelength on a WR3.4 rectangular waveguide, thus achieving high-gain beam steering over its operating sub-THz range. The measurement results show that the antenna achieves a reflection coefficient of less than -15 dB and a beam-steering range of -71° to -16° , as the operating frequency varies from 230 GHz to 330 GHz, respectively. The antenna is integrated with a conformal plano-convex parabolic lens, which is designed taking into consideration the phase center of multiple steered beams. The conformal-lens integration leads to an antenna gain enhancement of 5 dB to 10 dB over the complete beam-steering range. The conformal lens-integrated 2×32 E-slot WR3.4 antenna achieves a measured peak antenna gain of 30 dBi in the 230 GHz to 330 GHz range. A prototype of the conformal lens-integrated WR3.4 antenna is realized using a relatively low-cost manufacturing and assembly concept based on standard CNC milling and a laser ablation process, giving it a clear edge over previously demonstrated sub-THz rectangular waveguide beam-steering antennas manufactured using a high-precision silicon micromachining process. The overall size of the lens-integrated antenna is extremely compact, i.e., $65 \text{ mm} \times 30 \text{ mm} \times 32.35 \text{ mm}$. The conformal lens-integrated WR3.4 antenna can be easily connected to a sub-THz

wireless transmitter operating in a broad frequency range of 230 GHz to 330 GHz. The WR3.4 standard waveguide flange used in the antenna ensures a direct interface to a sub-THz wireless transmitter in a split-block waveguide package. Such a broadband sub-THz wireless transmitter-and-antenna module with a large beam-steering range and high gain can be used to establish a high-data-rate point-to-multipoint wireless link operating over several meters.

ACKNOWLEDGMENT

The authors would like to thank Mirko Nonnenmacher for CNC milling of the split-block module and the lens, and Thorsten Fux for laser ablation of the aluminum sheet.

REFERENCES

- [1] International Telecommunication Union - Radiocommunication Sector (ITU-R), "Future technology trends of terrestrial International Mobile Telecommunications systems towards 2030 and beyond", Report ITU-R M.2516-0, Nov. 2022. [Online]. Available: <https://www.itu.int/pub/R-REP-M.2516>. Accessed on: Feb. 18, 2024.
- [2] T. S. Rappaport et al., "Wireless Communications and Applications Above 100 GHz: Opportunities and Challenges for 6G and Beyond," in *IEEE Access*, vol. 7, pp. 78729-78757, 2019, doi: 10.1109/ACCESS.2019.2921522.
- [3] M. Giordani, M. Polese, M. Mezzavilla, S. Rangan and M. Zorzi, "Toward 6G Networks: Use Cases and Technologies," in *IEEE Communications Magazine*, vol. 58, no. 3, pp. 55-61, March 2020, doi: 10.1109/MCOM.001.1900411.
- [4] T. S. Rappaport, J. N. Murdock and F. Gutierrez, "State of the Art in 60-GHz Integrated Circuits and Systems for Wireless Communications," in *Proceedings of the IEEE*, vol. 99, no. 8, pp. 1390-1436, Aug. 2011, doi: 10.1109/JPROC.2011.2143650.
- [5] M. S. Shur and Jian-Qiang Lu, "Terahertz sources and detectors using two-dimensional electronic fluid in high electron-mobility transistors," in *IEEE Transactions on Microwave Theory and Techniques*, vol. 48, no. 4, pp. 750-756, April 2000, doi: 10.1109/22.841969.
- [6] H. -J. Song, K. Ajito, Y. Muramoto, A. Wakatsuki, T. Nagatsuma and N. Kukutsu, "Uni-Travelling-Carrier Photodiode Module Generating 300 GHz Power Greater Than 1 mW," in *IEEE Microwave and Wireless Components Letters*, vol. 22, no. 7, pp. 363-365, July 2012, doi: 10.1109/LMWC.2012.2201460.
- [7] V. Petrov, T. Kurner and I. Hosako, "IEEE 802.15.3d: First Standardization Efforts for Sub-Terahertz Band Communications toward 6G," in *IEEE Communications Magazine*, vol. 58, no. 11, pp. 28-33, November 2020, doi: 10.1109/MCOM.001.2000273.
- [8] I. Kalfass, F. Boes, T. Messinger, et al. 64 Gbit/s Transmission over 850 m Fixed Wireless Link at 240 GHz Carrier Frequency. *J Infrared Milli Terahz Waves* 36, 221-233 (2015). <https://doi.org/10.1007/s10762-014-0140-6>
- [9] H. Hamada et al., "300-GHz-Band 120-Gb/s Wireless Front-End Based on InP-HEMT PAs and Mixers," in *IEEE Journal of Solid-State Circuits*, vol. 55, no. 9, pp. 2316-2335, Sept. 2020, doi: 10.1109/JSSC.2020.3005818.
- [10] J. Dittmer, J. Tebart, C. Füllner, C. Koos, A. Stöhr and S. Randel, "200 Gbit/s Wireless THz Transmission over 52m using Optoelectronic Signal Generation," 2023 53rd European Microwave Conference (EuMC), Berlin, Germany, 2023, pp. 134-137, doi: 10.23919/EuMC58039.2023.10290657.
- [11] I. Dan, "A Comparison of System Architectures for Wireless Links in the Terahertz Band," PhD thesis, University of Stuttgart, Germany, 2022. [Online]. Available: <https://elib.uni-stuttgart.de/handle/11682/12406>. Accessed on: Feb. 18, 2024.
- [12] D. Müller et al., "A h-band reflective-type phase shifter MMIC for ISM-Band applications," 2014 IEEE MTT-S International Microwave Symposium (IMS2014), Tampa, FL, USA, 2014, pp. 1-4, doi: 10.1109/MWSYM.2014.6848423.
- [13] P. Lu et al., "InP-Based THz Beam Steering Leaky-Wave Antenna," in *IEEE Transactions on Terahertz Science and Technology*, vol. 11, no. 2, pp. 218-230, March 2021, doi: 10.1109/TTHZ.2020.3039460.
- [14] T. Haddad, C. Biurrun-Quel, P. Lu, H. Kaya, I. Mohammad and A. Stöhr, "Suppressing Open Stopband for Terahertz Periodic Microstrip Leaky-wave Antennas," 2023 17th European Conference on Antennas and Propagation (EuCAP), Florence, Italy, 2023, pp. 1-5, doi: 10.23919/EuCAP57121.2023.10132932.
- [15] A. Bhutani, M. Kretschmann, J. Dittmer, P. Lu, A. Stöhr, and T. Zwick, "A 220 GHz to 325 GHz Grounded Coplanar Waveguide Based Periodic Leaky-Wave Beam-Steering Antenna in Indium Phosphide Process," *Electronics* 2023, 12, 3482. <https://doi.org/10.3390/electronics12163482>
- [16] J. Tebart, J. Dittmer, T. Haddad, P. Lu, S. Randel and A. Stöhr, "Mobile 6G Communications at THz Frequencies Enabled by Leaky-wave Antenna Beam Steering," 2023 53rd European Microwave Conference (EuMC), Berlin, Germany, 2023, pp. 142-145, doi: 10.23919/EuMC58039.2023.10290642.
- [17] K. Sarabandi, A. Jam, M. Vahidpour and J. East, "A Novel Frequency Beam-Steering Antenna Array for Submillimeter-Wave Applications," in *IEEE Transactions on Terahertz Science and Technology*, vol. 8, no. 6, pp. 654-665, Nov. 2018, doi: 10.1109/TTHZ.2018.2866019.
- [18] D. Dancila, B. Beuerle, U. Shah, J. Oberhammer and A. Rydberg, "Leaky Wave Antenna at 300 GHz in Silicon Micromachined Waveguide Technology," 2019 44th International Conference on Infrared, Millimeter, and Terahertz Waves (IRMMW-THz), Paris, France, 2019, pp. 1-2, doi: 10.1109/IRMMW-THz.2019.8873927.
- [19] A. V. Boriskin, R. Sauleau, J. R. Costa and C. Fernandes, "Integrated Lens Antennas," in *Aperture Antennas for Millimeter and Sub-Millimeter Wave Applications*, 1st ed. Switzerland: Springer International Publishing AG, 2018, ch. 1, pp. 3-36.
- [20] N. T. Nguyen, A. V. Boriskin, L. Le Coq and R. Sauleau, "Improvement of the Scanning Performance of the Extended Hemispherical Integrated Lens Antenna Using a Double Lens Focusing System," in *IEEE Transactions on Antennas and Propagation*, vol. 64, no. 8, pp. 3698-3702, Aug. 2016, doi: 10.1109/TAP.2016.2572227.
- [21] J. R. Costa, E. B. Lima and C. A. Fernandes, "Compact Beam-Steerable Lens Antenna for 60-GHz Wireless Communications," in *IEEE Transactions on Antennas and Propagation*, vol. 57, no. 10, pp. 2926-2933, Oct. 2009, doi: 10.1109/TAP.2009.2029288.
- [22] L. Xue and V. Fusco, "Patch Fed Planar Dielectric Slab Extended Hemi-Elliptical Lens Antenna," in *IEEE Transactions on Antennas and Propagation*, vol. 56, no. 3, pp. 661-666, March 2008, doi: 10.1109/TAP.2008.916974.
- [23] L. Josefsson and S. R. Rengarajan, "The Slot Antenna," in *Slotted Waveguide Array Antennas Theory, Analysis and Design*, 1st ed. London, United Kingdom: Scitech Publishing, 2018, pp. 38. [Online]. Available: <https://digital-library.theiet.org/content/books/ew/sbaw517e>. Accessed on: Feb. 08, 2024.
- [24] H. Y. Yee and R. C. Voges, Texas Instruments Inc. "Slot Antenna Arrays" in *Antenna Engineering Handbook*, 3rd ed. United States of America: McGraw Hill Inc., 1993, ch. 9, pp. 9-1-9-39.
- [25] D. M. Pozar, "Transmission Lines and Waveguides," in *Microwave Engineering*, 3rd ed. United States of America: John Wiley and Sons, Inc., 2005, ch. 3, pp. 91-157.
- [26] K. W. Brown, "Design of waveguide slotted arrays using commercially available finite element analysis software," *IEEE Antennas and Propagation Society International Symposium. 1996 Digest*, Baltimore, MD, USA, 1996, pp. 1000-1003 vol.2, doi: 10.1109/APS.1996.549765.
- [27] A. Dion, "Nonresonant slotted arrays," in *IRE Transactions on Antennas and Propagation*, vol. 6, no. 4, pp. 360-365, October 1958, doi: 10.1109/TAP.1958.1144611.
- [28] L. Josefsson and S. R. Rengarajan, "Slot models," in *Slotted Waveguide Array Antennas Theory, Analysis and Design*, 1st ed. London, United Kingdom: Scitech Publishing, 2018, pp. 66-67. [Online]. Available: <https://digital-library.theiet.org/content/books/ew/sbaw517e>. Accessed on: Feb. 08, 2024.
- [29] B. Stöckel, "Quasi-optical measurement of complex dielectric constant at 300 GHz," *International Journal of Infrared and Millimeter Waves*, 1993, pp. 2131-2148 vol.14, <https://doi.org/10.1007/BF02096378>.
- [30] C. Gerhard, "Calculation of simple optical components and systems," in *Lens Design Basics*, 1st ed. Bristol, United Kingdom: IOP Publishing Ltd, 2020, ch. 3, pp. 3-1-3-18.
- [31] B. Goettel, P. Pahl, C. Kutschker, S. Malz, U. R. Pfeiffer and T. Zwick, "Active Multiple Feed On-Chip Antennas With Efficient In-Antenna Power Combining Operating at 200-320 GHz," in *IEEE Transactions*

- on Antennas and Propagation, vol. 65, no. 2, pp. 416-423, Feb. 2017, doi: 10.1109/TAP.2016.2634398.
- [32] M. J. M. van der Vorst, P. J. I. de Maagt and M. H. A. J. Herben, "Effect of internal reflections on the radiation properties and input admittance of integrated lens antennas," in IEEE Transactions on Microwave Theory and Techniques, vol. 47, no. 9, pp. 1696-1704, Sept. 1999, doi: 10.1109/22.788611.
- [33] J. Auerswald, A. Rucklia, T. Gschwilma, P. Weber, D. Diego-Vallejo, and H. Schlüter, "Taper angle adjustment in ultra-short pulse laser cutting of complex micro-mechanical contours," in 9th International Conference on Photonic Technologies LANE 2016, Industrial Paper published by Bayerisches Laserzentrum GmbH, 2016
- [34] H. Gulan et al., "Probe based antenna measurements up to 325 GHz for upcoming millimeter-wave applications," 2013 International Workshop on Antenna Technology (iWAT), Karlsruhe, Germany, 2013, pp. 228-231, doi: 10.1109/IWAT.2013.6518338.
- [35] S. Beer and T. Zwick, "Probe based radiation pattern measurements for highly integrated millimeter-wave antennas," Proceedings of the Fourth European Conference on Antennas and Propagation, Barcelona, Spain, 2010, pp. 1-5.



Akanksha Bhutani (Senior Member, IEEE) obtained her M.Sc. and Ph.D. degrees in Electrical Engineering and Information Technology from the Karlsruhe Institute of Technology (KIT), Germany, in 2012 and 2019, respectively. From 2012 to 2019, she served as a Research Associate at the Institute of Radio Frequency Engineering and Electronics (IHE), KIT. Since 2021, she has been leading the Antennas and Packaging research group at IHE, KIT. Her primary research revolves around sub-THz antennas and packaging for radar and

wireless communication systems. Her contributions have garnered notable recognition, including the "Carl Freudenberg Prize" and the "Suedwestmetall Advancement Award" for her outstanding dissertation in 2019 and 2020, respectively. Additionally, she received the IEEE Microwave Magazine Best Paper Award in 2017 and the European Microwave Week (EuMW) Best Paper Awards in 2019 and 2022. In 2023, she served as the Operations Officer at EuMW 2023, held in Berlin. Later that year, she was honored with the prestigious International IHP "Wolfgang Mehr" Fellowship Award by the Leibniz Institute for High Performance Microelectronics (IHP). She has authored and co-authored over 60 research papers published in peer-reviewed conference proceedings and scientific journals.



Joel Dittmer (Student Member, IEEE) was born in Karlsruhe, Germany, in 1995. He received the B.Sc. and M.Sc. degrees in electrical engineering from the Karlsruhe Institute of Technology, Karlsruhe, Germany, in 2020 and 2022, respectively. He joined the Institute of Photonics and Quantum Electronics (IPQ) at the Karlsruhe Institute of Technology in 2023, where he started as a research assistant in the field of optoelectronic and electronic generated Terahertz signals for wireless communications. His research interests include

THz system design, THz package design, and high data rate digital signal processing.



Luca Valenziano (Student Member, IEEE) received the master's degree in electrical engineering from the University of Applied Sciences Karlsruhe (HKA), Karlsruhe, Germany, in 2022. He is currently working as a Research Associate with the Institute of Radio Frequency Engineering and Electronics (IHE), Karlsruhe Institute of Technology (KIT). His main fields of research interests focus on concepts for millimeter-wave (mmW) packaging and ultra-broadband packaging of electro-optical systems.



Thomas Zwick (Fellow, IEEE) received the Dipl.-Ing. (M.S.E.E.) and the Dr.-Ing. (Ph.D.E.E.) degrees from the Universität Karlsruhe (TH), Germany, in 1994 and 1999, respectively. From 1994 to 2001 he was a research assistant at the Institut für Höchstfrequenztechnik und Elektronik (IHE) at the Universität Karlsruhe (TH), Germany. In February 2001 he joined IBM as research staff member at the IBM T. J. Watson Research Center, Yorktown Heights, NY, USA. From October 2004 to September 2007, Thomas Zwick was with

Siemens AG, Lindau, Germany. During this period he managed the RF development team for automotive radars. In October 2007, he became a full professor at the Karlsruhe Institute of Technology (KIT), Germany. He is the director of the Institut für Hochfrequenztechnik und Elektronik (IHE) at the KIT.

Thomas Zwick is author or co-author of over 400 technical papers and 20 patents. Together with his team he received over 20 best paper awards on international conferences. He served on the technical program committees (TPC) of several scientific conferences. In 2013 Dr. Zwick was general chair of the international Workshop on Antenna Technology (iWAT 2013) in Karlsruhe and in 2015 of the IEEE MTT-S International Conference on Microwaves for Intelligent Mobility (ICMIM) in Heidelberg. He also was TPC chair of the European Microwave Conference (EuMC) 2013. In 2017 he was General TPC Chair of European Microwave Week. From 2008 until 2015 he has been president of the Institute for Microwaves and Antennas (IMA). T. Zwick became selected as a distinguished microwave lecturer for the 2013 – 2015 period with his lecture on "QFN Based Packaging Concepts for Millimeter-Wave Transceivers". Since 2017 he is member of the Heidelberg Academy of Sciences and Humanities. In 2018 Thomas Zwick became appointed IEEE Fellow, since 2019 he is member of acatech. In 2022 he was awarded an honorary doctorate of the Faculty of Electrical Engineering and Informatics at the Budapest University of Technology and Economics in Hungary.